J Mater Sci: Mater Electron (2021) 32:16945–16955

Temperature sensitivity and electrical stability of Sb/Mn co-doped SnO_2 ceramics

Guoxiang Jiang[1], Zhicheng Li[1], Chang You[1], Wenbin Hao[1], Zhiyuan Ma[2], and Hong Zhang[1,*]

[1] School of Materials Science and Engineering, Central South University, Changsha 410083, China
[2] School of New Energy and Materials, Southwest Petroleum University, Chengdu 610500, China

Received: 20 March 2021
Accepted: 21 May 2021
Published online: 2 June 2021

ABSTRACT

SnO_2-based ceramics ($Sn_{1-x}Sb_xO_2$, $0 \le x \le 0.06$, denoted as xATO; $Sn_{0.95-y}Sb_{0.05}Mn_yO_2$, $0 \le y \le 0.05$, denoted as yMATO) were prepared by solid-state reaction method. XRD analysis revealed that all ceramics contain rutile-type crystalline structure and no impurity was detected. The effect of Sb and Mn doping on temperature sensitivity and electrical stability of the ceramics were investigated. yMATO ceramics show typical NTC behavior contributed from both grain and grain boundary effect. The room-temperature resistivities from 3.88 Ω cm to 38.5 kΩ cm and temperature sensitivity constants ($B_{25/85}$) from 288 to 5808 K can be adjusted by altering the content of Mn ions. Mn doping can enhance the electrical stability of the ceramics, the aging-induced resistivity change rate is 0.6% of 0.04MATO ceramic after being aged at 150 °C for 500 h, while 0.05ATO ceramic without Mn doping has resistance change rate of − 14.29%.

1 Introduction

Due to the unique performance, like high sensitivity, fast response, and low cost, negative temperature coefficient (NTC) thermistors are playing important role in industrial and domestic aspects, such as temperature sensing, temperature compensation, circuit protection, infrared detection, and infrared imaging [1–5]. The most commonly used NTC thermistors are spinel-type transition metal oxides with general formula, like AB_2O_4, such as Mn–Ni–O, Mn–Fe–O, Mn–Co–Ni–O, Mn–Co–Fe–Ni–O, and Mn–Ni–Co–Cu–Zn–O systems [6–12]. In practice, the electrical properties of NTC thermistors are generally characterized by room-temperature resistivity (ρ_{25}) and temperature sensitivity constant (B value). Controllable ρ_{25} and B values are required for diverse products in practical applications.

In the meanwhile, the electrical stability of NTC thermistors is also one of the key properties for practical applications. Nowadays, investigations on aging characteristics are mainly focused on spinel oxides, in which the aging induced resistance change was generally considered to be the rearrangement and/or redox reaction of the cations [13–16]. Battault et al. pointed out that the aging origin in

Address correspondence to E-mail: hzhang@csu.edu.cn

https://doi.org/10.1007/s10854-021-06258-x

$Mn_{2.42}Fe_{0.58}O_4$ thermistor was closely related to the migration and rearrangement of Fe^{3+} and Mn^{2+} ions between tetrahedral and octahedral sites in spinel structure [17]. Groen et al. found that oxidation reaction occurred at grain boundaries and the resulting cationic vacancies migration from grain boundaries to grains during aging process was responsible for aging deterioration in Mn–Ni–Fe–O system [18]. Furthermore, the poor sinterability of ceramics, ion oxidation, and the reconfiguration of electrode/ceramic interface may also result in aging deterioration [19–21]. Several strategies have been employed to improve the electrical stability of the thermistors. Li et al. fabricated $Mn_{1.95-x}Co_{0.21}Ni_{0.84}Na_xO_4$ thermistors with excellent stability for that the second phase $Na_{0.7}MnO_{2.05}$ can block the transport of oxygen vacancies [22]. Guan et al. reported that Fe doping can improve the electrical stability of $LaCrO_3$, with the resistance shifts less than 0.65% [23].

Recent years, NTC thermistors based on single cation oxides, such as SnO_2, ZnO, CuO, and NiO, have attracted attentions [24–28]. Those single cation oxides have unique advantage that ρ_{25} and B value can be effectively adjusted by suitable ionic doping. For example, Yang et al. reported a thermo-sensitive NiO-based ceramic, where ρ_{25} from 47 Ω cm to 1 MΩ cm and $B_{25/85}$ values from 2582 to 8019 K were obtained by modifying the concentration of B^{3+} and Na^+ ions [27]. Some works based on SnO_2-based ceramics have been reported, e.g., Sb-doped SnO_2 oxides modified by Zr, Ti, Fe, or Cr ions, all of which showed excellent NTC characteristics [24, 29–31].

Despite of high adjustability of ρ_{25} and B value, the demand for high electrical stability is increasing. However, there has been little detailed work on the electrical stability of NTC thermistors based on those single cation oxides. In this work, Sb-doped SnO_2 ceramics modified by Mn ion were prepared. The results show that the Sb/Mn co-doped SnO_2 ceramics have controllable ρ_{25} and B value, and high electrical stability can be received with appropriate content of Mn ions.

2 Experimental

Sb/Mn co-doped SnO_2 ceramics with nominal formula of $Sn_{1-x-y}Sb_xMn_yO_2$ (x = 0, 0.01, 0.03, 0.05, and 0.06, denoted as xATO; y = 0, 0.01, 0.02, 0.03, 0.04, 0.045, and 0.05, denoted as yMATO) were synthesized by solid-state reaction method. The raw materials are tin oxide (SnO_2, Xilong Scientific, China), antimony oxide (Sb_2O_3, Xilong Scientific, China), and manganese dioxide (MnO_2, Hengxing chemical reagent manufacturing, China). Appropriate amount of the raw materials were weighed according to the nominal formula of $Sn_{1-x-y}Sb_xMn_yO_2$ and were mixed by ball milling for 1 h in deionized water. The mixed slurries were dried at 110 °C for 12 h. Then the dried mixtures were calcined at 900 °C for 5 h in air. For each batch, 2% (weight ratio) of CuO (Xilong Scientific, China) was added as the sintering aid in the calcined powders. The mixture was granulated with polyvinyl alcohol (PVA) solution and then was pressed into pellets with a diameter of 12 mm and thickness of about 3 mm. The green pellets were sintered at 1250 °C for 1 h in air for the yMATO samples, while the samples without Mn dopant were sintered at 1300 °C for 1 h in air. For electrical property measurement, two opposite surfaces of the as-sintered ceramics were polished and were brushed with silver paste. The silver coating was subsequently cured at 600 °C for 5 min to formed ohmic electrodes.

The phase composition and lattice parameters of the as-sintered ceramics were characterized by using X-ray diffractometer (XRD, Rigaku D/Max 2500, Japan) with Cu K_α radiation (λ = 0.154056 nm) in diffract angle (2θ) ranges between 10° and 90° at a scanning rate of 8° min^{-1}. For microstructure observation, the as-sintered ceramics were broken into pieces, and the morphology of fracture surfaces were observed using a scanning electron microscopy (SEM, JEOL JSM 7900F). Energy dispersive X-ray spectroscopy (EDS, Oxford Ultim Max 65) attached to the SEM was employed to analyze the elemental distributions in ceramics. X-ray photoelectron spectroscopy (XPS, K-alpha 1063, UK) was used for detecting the valence states of cations in ceramics. The densities of all ceramics were obtained by the Archimedes method in water; the relative density was calculated from the ratio between measured density and theoretical density of the ceramics, i.e., $D_r = D_m/D_l$, where D_r is relative density, D_m is measured density, and D_l is lattice density.

Resistance–temperature data (R–T) of the specimens were recorded by using a resistance–temperature measurement system (ZWC-C, Huazhong University of Science and Technology, China) under direct current (DC) condition in temperature range

from 25 to 250 °C. The resistivity (ρ) was calculated based on the measured resistance (R) according to the equation of $\rho = R(S/h)$, where S and h are, respectively, electrode area (cm^2) and thickness (cm) of the measured sample. Alternating current (AC) impedance measurement was carried out by using an electrochemical measurement system (Gamry Reference 600, USA) in a frequency range from 1 Hz to 1 MHz, and the impedance data were analyzed by Gamry Echem Analyst program.

For investigation of electrical stability, aging treatment was conducted at 150 °C in air by putting the samples with ohmic electrodes in an oven. After being aged for 50 h, the samples were taken out from the oven and were put in an ambient-temperature (25 °C) room for more than 1 h before the resistance measurement. After resistance measurement, the samples were placed back into oven for further aging treatment. This process was repeated ten times and the aging duration was accumulated to 500 h. The resistance change rate is given by $\Delta R/R_0 = (R_i - R_0)/R_0$, in which R_0 is resistance measured at 25 °C before aging treatment and R_i is resistance measured at 25 °C after each stage aging treatment.

3 Results and discussion

3.1 Phase and microstructure

Figure 1 shows the XRD patterns of the as-sintered $Sn_{1-x-y}Sb_xMn_yO_2$ ceramics with various contents of Sb- and Mn- dopants. All the diffraction peaks can be assigned to tetragonal rutile structure with a space group of $P4_2/mnm$ (136) (referred by PDF No. 41-1445, $a = b = 0.4738$ nm, $c = 0.3187$ nm). No impurity peak was detected. These indicate that Mn, Sb, and Cu ions have substituted into the SnO_2 lattice, or the content of impurity phase is too small to be detected.

Refined by Jade 6.0+pdf2004 program, the lattice parameters for the prepared ceramics are listed in Table 1. The lattice parameters of 0ATO ceramic ($a = 0.4731$ nm, $c = 0.3182$ nm) are slightly smaller than those referred to the PDF no. 41-1445. It may result from the formation of oxygen vacancies for insufficient oxygen in the sintering environment and for the introduction of CuO that substitutes into the ATO lattice and produce oxygen vacancies. The

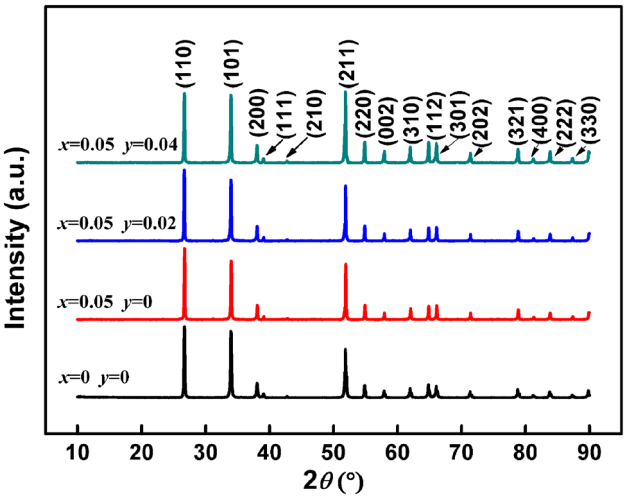

Fig. 1 X-ray diffraction patterns of the as-sintered $Sn_{1-x-y}Sb_xMn_yO_2$ ceramics

lattice parameters of 0.05ATO ceramic are smaller than that of 0ATO. During the calcination and sintering processes, Sb^{3+} ion could be oxidized to Sb^{5+} ion. The ionic radius of Sb^{5+} (0.061 nm) is smaller than those of Sn^{4+} ion (0.069 nm) and Cu^{2+} (0.073 nm), resulting in decrease of lattice parameters.

When Mn ions was introduced into Sb-doped SnO_2 compounds, the related c lattice parameters decreased slightly with the rise of Mn ions concentrations. The Mn ions may have Mn^{2+} (0.066 nm), Mn^{3+} (0.058 nm), and Mn^{4+} (0.053 nm) ions, which can be confirmed by later XPS analysis. The ionic radii of most Mn ions are smaller than those of Sn^{4+}, Sb^{5+}, Sb^{3+}, and Cu^{2+} ions, leading to c lattice parameters decrease in yMATO ceramics.

SEM images of the as-sintered ceramics of 0ATO, 0.05ATO, 0.02MATO, and 0.04MATO are shown in Fig. 2. As shown in Fig. 2a, the 0ATO ceramic shows inhomogeneous particle size and some small pores. For the 0.05ATO ceramic, as shown in Fig. 2b, the average grain size is about 1–2 μm, and the grains contacted each other tightly. Figure 2c and d shows that the grain sizes slightly increased with the increase of Mn content in Mn-doped ATO ceramics.

Figure 3a shows a secondary electron SEM image of a 0.04MATO ceramic. Elemental distributions of the area in Fig. 3a are shown in Fig. 3b–e. The results show that homogeneous elemental distribution of Sn, Sb, Mn, and O exists in 0.04MATO ceramic.

The relative densities of 0ATO, 0.05ATO, 0.02MATO, and 0.04MATO ceramics were measured

Table 1 Lattice parameters, measured densities D_m, lattice densities D_l, and relative densities D_r of the as-sintered $Sn_{1-x-y}Sb_xMn_yO_2$ ceramics with different contents of Sb and Mn ions

Sample	$a = b$ (nm)	c (nm)	D_m (g cm^{-3})	D_l (g cm^{-3})	D_r (%)
0ATO	0.4731	0.3182	6.2320	7.0300	88.6
0.05ATO	0.4727	0.3181	6.7259	7.0510	95.4
0.02MATO	0.4729	0.3180	6.5332	6.9880	93.5
0.04MATO	0.4728	0.3179	6.5508	6.9340	94.5

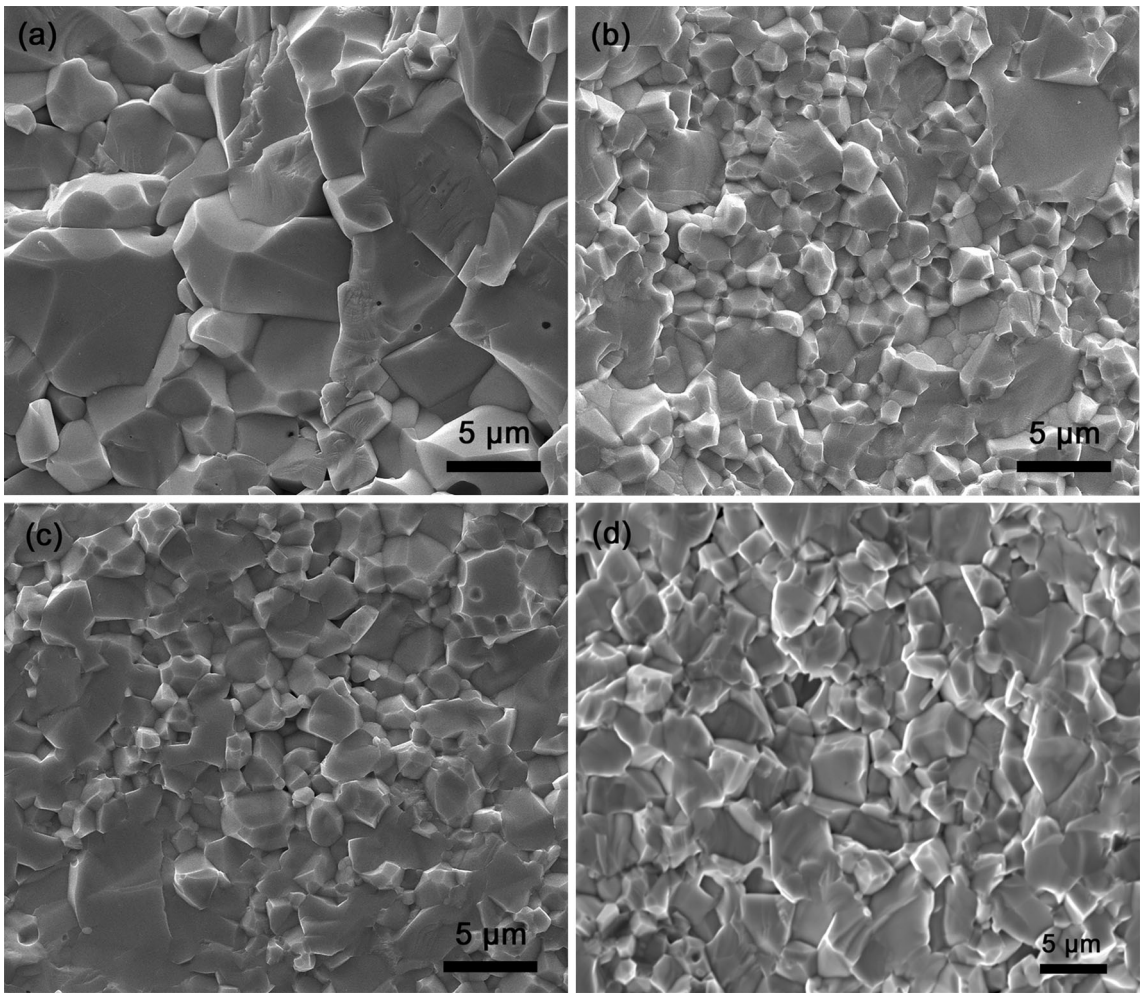

Fig. 2 SEM images of cross-sectional view of SnO_2-based ceramics, **a** 0ATO, **b** 0.05ATO, **c** 0.02MATO, **d** 0.04MATO

by Archimedes displacement method and were calculated by comparing the measured density D_m to lattice density D_l. The lattice density of each ceramic can be calculated by $D_l = MZ/N_AV$, where M is molecular weight, Z is number of atoms per unit cell ($Z = 2$ for SnO_2), N_A is the Avogadro constant, and V is volume of unit cell ($V = a^2c$ for SnO_2). The results are shown in Table 1. The Sb/Mn co-doped SnO_2 ceramics have high relative densities of 95.4% (0.05ATO), 93.5% (0.02MATO), and 94.5% (0.04MATO).

3.2 Electrical properties

The undoped SnO_2 ceramic has a high room-temperature resistivity (ρ_{25}) of 0.13 MΩ cm. However, Sb doping reduced obviously ρ_{25} of SnO_2-based ceramics. ρ_{25} of xATO ceramics are 9.41 Ω cm for $x = 0.01$, 6.09 Ω cm for $x = 0.03$, 3.88 Ω cm for $x = 0.05$ and 6.67 Ω cm for $x = 0.06$, respectively. These results are in agreement with the previous reports [30, 31]. When the content of Sb_2O_3 is low, majority of Sb^{3+} ion could be oxidized to Sb^{5+} ion during calcination and

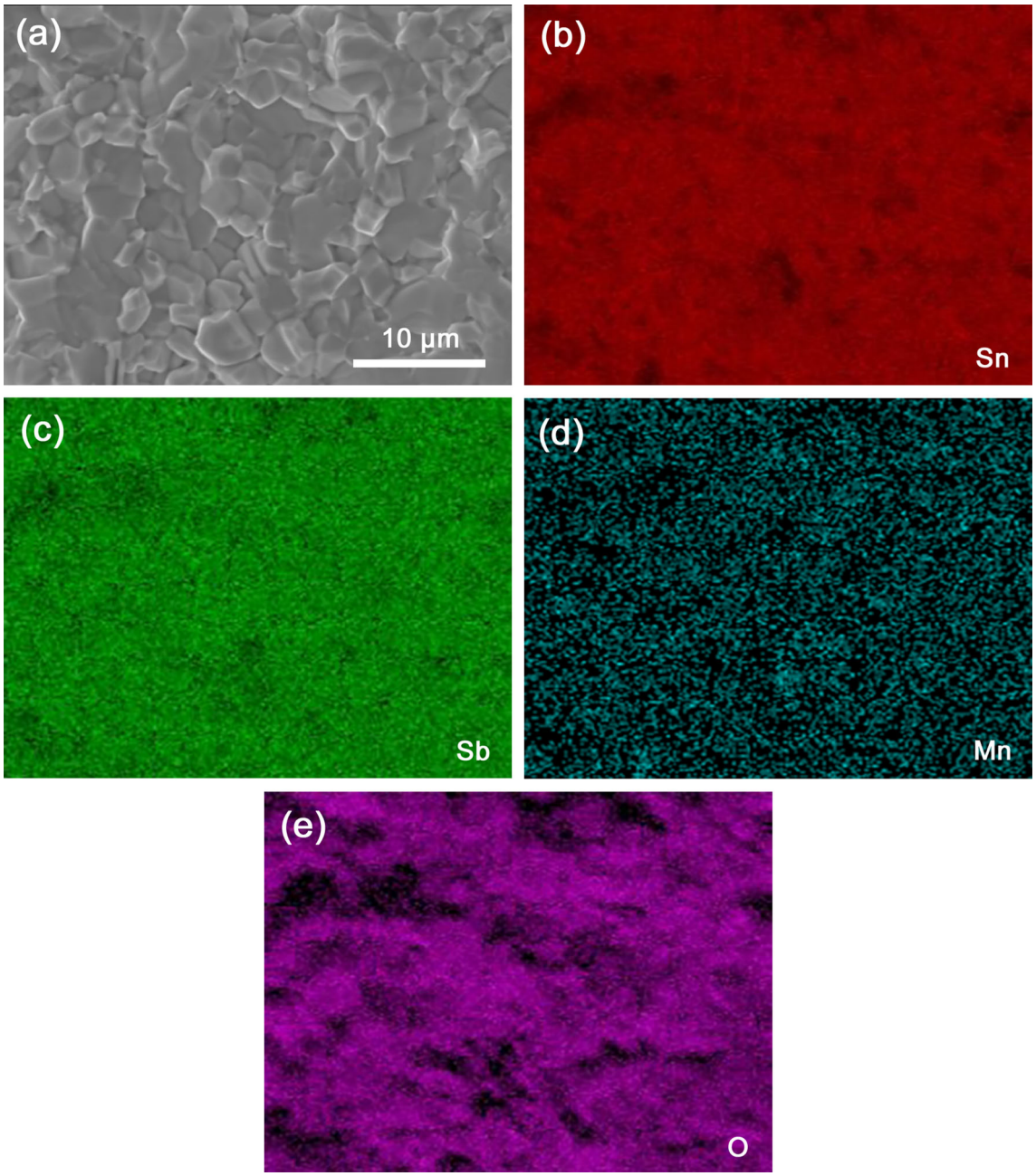

Fig. 3 EDS analysis of elemental distribution in 0.04MATO ceramic, **a** secondary electron SEM image, **b** Sn element mapping, **c** Sb element mapping, **d** Mn element mapping, **e** O element mapping

sintering processes. Then Sb^{5+} ion acted as donor and introduced weakly bound electrons (charge carriers) as shown in Eq. (1). The weakly bound electrons can be thermal activated and jump to conduction band from the donor level, leading to decrease of resistivity.

$$Sb_2O_5 \xrightarrow{SnO_2} 2Sb_{Sn}^{\cdot} + 2e' + 4O_O + \frac{1}{2}O_2. \quad (1)$$

For a semiconductor material, there is appropriate doping concentration to get the lowest resistivity. With further increase of Sb_2O_3 content, more Sb^{3+} ions were retained and acted as acceptors in SnO_2-based ceramic. As a result, the electron holes occurred and locate at the acceptor level near the valence

band. Then the electron holes captured the weakly bound electrons produced by Sb^{5+} ion, and decreased the concentration of weakly bound electrons, resulting in increase of resistivity.

In order to investigate the electrical property of the ATO-based ceramics, various contents of MnO_2 were introduced into $Sn_{0.95}Sb_{0.05}O_2$ ceramic in this work. The temperature dependence of resistivity in Arrhenius plots of yMATO ceramics with various contents of Mn ions are shown in Fig. 4a, indicating that the yMATO ceramics have typical NTC characteristic. The $\ln\rho$–$1000/T$ relationship can be nearly expressed by the Arrhenius law as shown in Eq. (2):

$$\rho = \rho_0 \exp\left(\frac{E_a}{kT}\right) = \rho_0 \exp\left(\frac{B}{T}\right), \quad (2)$$

where ρ is resistivity at temperature T (in Kelvin), ρ_0 is a pre-exponential factor relating to the material characteristic, E_a is activation energy of conduction, and k is the Boltzman constant. B is a material constant representing temperature sensitivity of a NTC thermistor. B value can be calculated by Eq. (3)

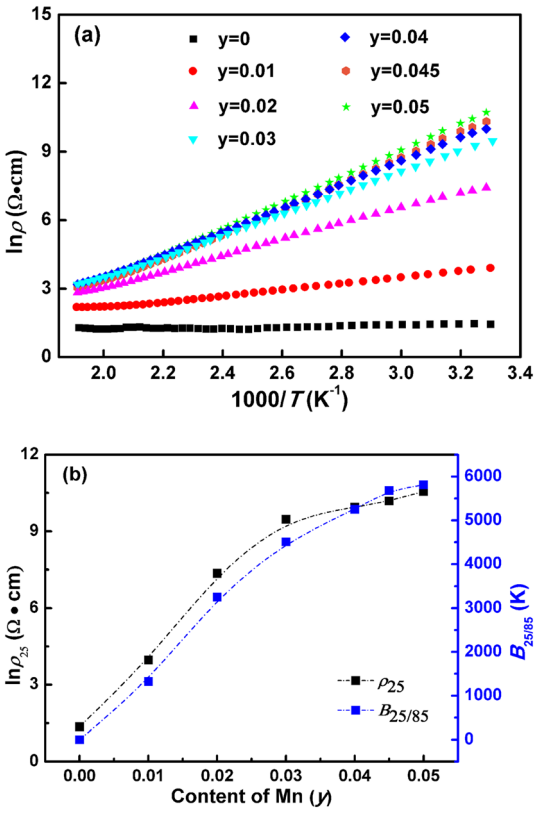

Fig. 4 Electrical properties of the as-sintered yMATO ceramics, **a** plots of $\ln\rho$—$1000/T$, **b** Mn concentration dependence of ρ_{25} and $B_{25/85}$

$$B_{25/85} = \frac{\ln\rho_{25} - \ln\rho_{85}}{1/T_{25} - 1/T_{85}}, \quad (3)$$

where ρ_{25} and ρ_{85} are the resistances at temperature of 298 K (25 °C) and 358 K (85 °C), respectively. So the B value is also denoted as $B_{25/85}$. ρ_{25} and $B_{25/85}$ of yMATO ceramics as function of Mn ion concentration is shown in Fig. 4b. ρ_{25} and $B_{25/85}$ increased monotonically with the increase of Mn ion content. For y is equal to 0.01, 0.02, 0.03, 0.04, 0.045, and 0.05, ρ_{25} is 0.053, 1.57, 12.9, 20.8, 26.5 and 38.5 kΩ cm and $B_{25/85}$ is 1537, 3253, 4507, 5252, 5682, and 5808 K, respectively. The adjustable ρ_{25} and $B_{25/85}$ values of yMATO system may meet various requirements in practical application.

As previous reports on the NTC thermistors based on single cation oxides [24–28], besides the band conduction contributed by donor or acceptor doping, polaron hopping is also one of the important conduction modes. The Mn-free ATO ceramics display high conductivity for donor doping of Sb^{5+} ions as shown in Eq. (1). The primary charge carriers in xATO are weakly bound electrons, and the main conduction mode in xATO should be the band conduction. When Mn ions substituted into the ATO lattice, the electrons at donor level are not only thermally activated to conduction level for electrical conductivity but also can be weakly bounded by Mn ions followed by formation of Mn^{3+} and Mn^{2+} ions. For different valent cations exist at the Sn sites in ATO, polaron hopping, such as $Mn^{4+} \leftrightarrow Mn^{3+} \leftrightarrow Mn^{2+}$, may take place to contribute to the hopping conduction. The polaron hopping must overcome the lattice barriers, leading to high activation energy of conduction and high B values. In the meanwhile, the concentration of the electron charge carriers decreased with the increase of Mn ions content, resulting in the increase of ρ_{25}.

3.3 AC impedance analysis

Complex impedance spectrum (CIS) is employed to characterize the electrical properties. Generally, an ideal CIS consists of three semicircles, which are associated with grain effect, grain boundary effect, and electrode polarization effect, respectively. Figure 5 shows the Nyquist plots of yMATO ceramics measured at room temperature. Each CIS looks like to be composed of only one arc. An equivalent circuit $R_0(R_g\text{-}CPE_g)(R_{gb}\text{-}CPE_{gb})$ (as shown in the inset in

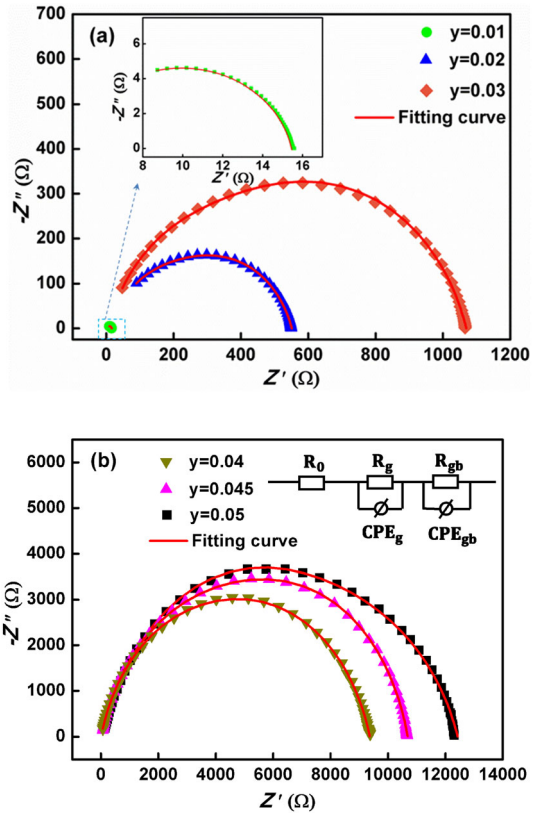

Fig. 5 Nyquist plots of *y*MATO ceramics modified with various content of Mn ions, measured at room temperature, **a** $y = 0.01$, 0.02, 0.03, **b** $y = 0.04$, 0.045, 0.05. The inset in Fig. 6b shows an equivalent circuit for data fitting

Fig. 5b) was utilized to fit the measured impedance data. Here, R_0, R_g, and R_{gb} represent electrode contact resistance, grain resistance, and grain boundary resistance, respectively. *CPE* is a constant phase element used to replace the capacitor to accommodate the non-ideal Debye behavior. The capacitance (C) of each part can be calculated by the fitted resistance and CPE, i.e., $C = Q^{1/n}R^{(1-n)/n}$, where Q is CPE parameter; n is a variable value related to the deviation from ideal Debye behavior, $n = 0$ for ideal resistor, $n = 1$ for ideal capacitor [32]. In Fig. 5, the measured data are marked by scattered symbolic points, and the curves are fitted to results by equivalent circuit. The fitting curves are in good agreement with the measured data. The relevant fitted results are also listed in Table 2. One can get that the grain effect and grain boundary effect co-contribute to the electrical properties.

Table 2 CIS fitted results of *y*MATO ceramics modified with various contents of Mn ions, grain resistance (R_g), grain capacitance (C_g), grain boundary resistance (R_{gb}), and grain boundary capacitance (C_{gb})

Sample	R_g (Ω)	C_g (nF)	R_{gb} (Ω)	C_{gb} (nF)
$y = 0.01$	4.1	0.16	10.9	19.8
$y = 0.02$	183.3	1.76	350.2	5.91
$y = 0.03$	319.7	3.15	742.2	9.83
$y = 0.04$	3838	2.86	5519	8.79
$y = 0.045$	4918	3.60	5745	13.00
$y = 0.05$	7631	2.60	4721	27.20

3.4 Aging behavior

The plots of aging time dependence of resistance change rates ($\Delta R/R_0$) of *y*MATO ceramics ($y = 0$, 0.01, 0.02, 0.03, 0.04, 0.045, and 0.05) are shown in Fig. 6. In the initial aging stage (about 50 h), all samples show negative resistance change rate, i.e., resistance decreased after aging 50 h. Then, 0MATO ceramic became stable. The 0MATO ceramic has final $\Delta R/R_0$ value of -14.29% after aging for 500 h. However, the resistances of *y*MATO ceramics ($y > 0$) increased in aging time from 50 to 200 h and the $\Delta R/R_0$ values are positive. After 200 h aging treatment, all samples (except the 0.05MATO) became gradually stable. The 0.04MATO ceramic has the lowest resistance change rates ($\Delta R/R_0$) of 0.6% after 500 h aging. Table 3 lists the aging performance of some ambient-temperature NTC thermistors reported in recent years. The resistance change rate of NTC thermistors with high aging stability usually limited to less than 2% [13, 14, 23, 26, 28, 33–35]. These indicated that thermistor with excellent aging stability can be obtained in *y*MATO ceramics.

To investigate the possible aging behavior, the valence states of Sb and Mn elements in *y*MATO ceramics ($y = 0$ and 0.04) were analyzed by XPS before and after aging. The fitted XPS spectra before aging and after 500 h aging are shown in Fig. 7. The C 1s peak located at 284.8 eV acts as a reference for binding energy calibration of the XPS analysis. In Fig. 7a, b, Sb $3d_{3/2}$ can be convoluted into two peaks, and the binding energy peaks locate at 539.2–539.4 and 539.9–540.1 eV. The two peaks can be attributed to Sb^{3+} and Sb^{5+} states [36], respectively. In Fig. 7c, the peaks locating at 639.8–639.9, 640.9–640.8, and

Table 3 Comparison of aging performance in various ambient-temperature NTC thermistors reported in recent years

NTC thermistors	Aging condition	$\Delta R/R_0$ (%)	$(\Delta R/R_0)_{min}$ (%)	References
$Zn_{0.2}Fe_{1.05}NiMn_{0.75}O_4$	125 °C/600 h	0.58–0.78	0.58	[33]
$Mn_{1.5-x}Co_{1.2}Cu_{0.3}Zn_xO_4$	125 °C/500 h	1.13–2.7	1.13	[34]
$Zn_{0.4}Fe_{2.1}Co_2Mn_{1.5}O_8$ films	125 °C/500 h	1.02–9.53	1.02	[35]
$LaCr_{1-x}Fe_xO_3$	125 °C/1000 h	< 0.65	/	[23]
Al/La/Cu-modified ZnO	125 °C/600 h	0.74–1.57	0.74	[26]
$Mn_{1.1}Co_{1.5}Fe_{0.4}O_4$	200 °C/800 h	0.5–15.1	0.5	[14]
Bi-modified $(Zn_{0.4}Ni_{0.6})_{1-x}Na_xO$	150 °C/700 h	1.8–237	1.8	[28]
$Mn_{1.95}Co_{0.21}Ni_{0.84}O_4@Al_2O_3$	125 °C/1000 h	2.22–2.34	0.59	[13]
Sb/Mn co-doped SnO_2	150 °C/500 h	− 14.29 to 7.9	0.6	This work

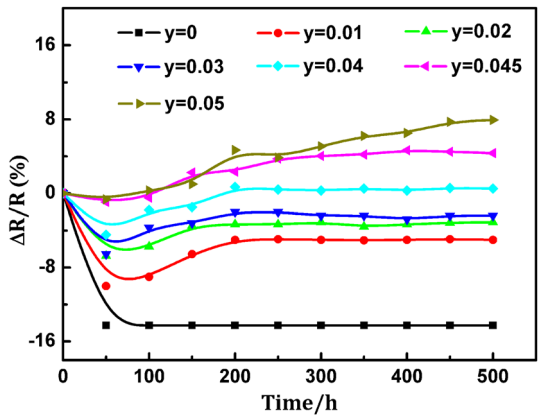

Fig. 6 Effect of Mn content on the resistance change rate $\Delta R/R$ of yMATO (y = 0, 0.01, 0.02, 0.03, 0.04, 0.045, 0.05) ceramics during the aging process treated at 150 °C

642.0–642.1 eV were assigned to reflect from Mn^{2+}, Mn^{3+}, and Mn^{4+}, respectively [37].

For y = 0 (0.05ATO without Mn doping) ceramic, as shown in Fig. 7a, the ratio of ionic concentration of $[Sb^{3+}]/[Sb^{5+}]$ was calculated to be 0.75 before aging. But the ratio decreased to 0.56 after aging. These indicate that the concentration of Sb^{3+} ion decreased during aging. So the origin of resistance decrease of 0.05ATO ceramic might be result from the oxidation reaction when the ceramics exposed in air for aging test. Generally, the surface of ceramic may adsorb oxygen molecules. According to the reports by Dai et al. [38], oxygen molecules (O_2) in atmospheric environment adhere to crystal surface, then may capture electrons from ceramic surfaces and interfaces (also be grain boundaries) to turn into the adsorbed oxygen (O_{ad}^{n-}, n ≤ 2). For the existence of oxygen vacancies inside grains and/or at grain boundaries in the ceramic, it is possible for O_{ad}^{n-} diffusing into the ceramic. As result, partial Sb^{3+} ion might be oxidized to Sb^{5+} ion. The increase of Sb^{5+} ionic concentration can induce more weakly bound electrons, resulting in the decrease of resistivity.

For 0.04MATO ceramic, as shown in Fig. 7b, the ration of ionic contents $[Sb^{3+}]/[Sb^{5+}]$ is 0.81 before aging, while the one is 0.72 after aging. The decrement in ionic ratios is smaller than that in 0.05ATO ceramic. On the other hand, as calculated from the XPS spectra as shown in Fig. 7c, the content percentages of Mn^{2+}, Mn^{3+}, and Mn^{4+} ions in the sample before aging are, respectively, 17.24%, 26.06%, and 56.70%, while the ones became to be, respectively, 4.69%, 21.78%, and 73.53% after aging. Obviously, the content of Mn^{4+} ion increased, and the ones of Mn^{3+} and Mn^{2+} ions decreased. With the introduction of Mn ion in the ceramics, Mn^{3+} and Mn^{2+} ions were oxidized to higher valence state with aging. These processes would restrain the oxidation of Sb^{3+} ion and reduced the resistance change of samples during aging. At the same time, the decrease of Mn^{2+} and Mn^{3+} concentrations leads to the decrease of Mn^{2+}/Mn^{3+} and Mn^{3+}/Mn^{4+} ion pairs, and reduces the effective sites for hopping conduction model. Thus, resistances of Mn-doped ceramics increased at the aging period of 50 to 200 h. It is concluded that the addition of MnO_2 could improve the electrical stability by suppressing the oxidation of Sb ion.

4 Conclusions

A series of SnO_2-based ceramics ($Sn_{1-x}Sb_xO_2$, $0 \le x \le 0.06$; $Sn_{0.95-y}Sb_{0.05}Mn_yO_2$, $0 \le y \le 0.05$) were successfully synthesized by conventional solid-state

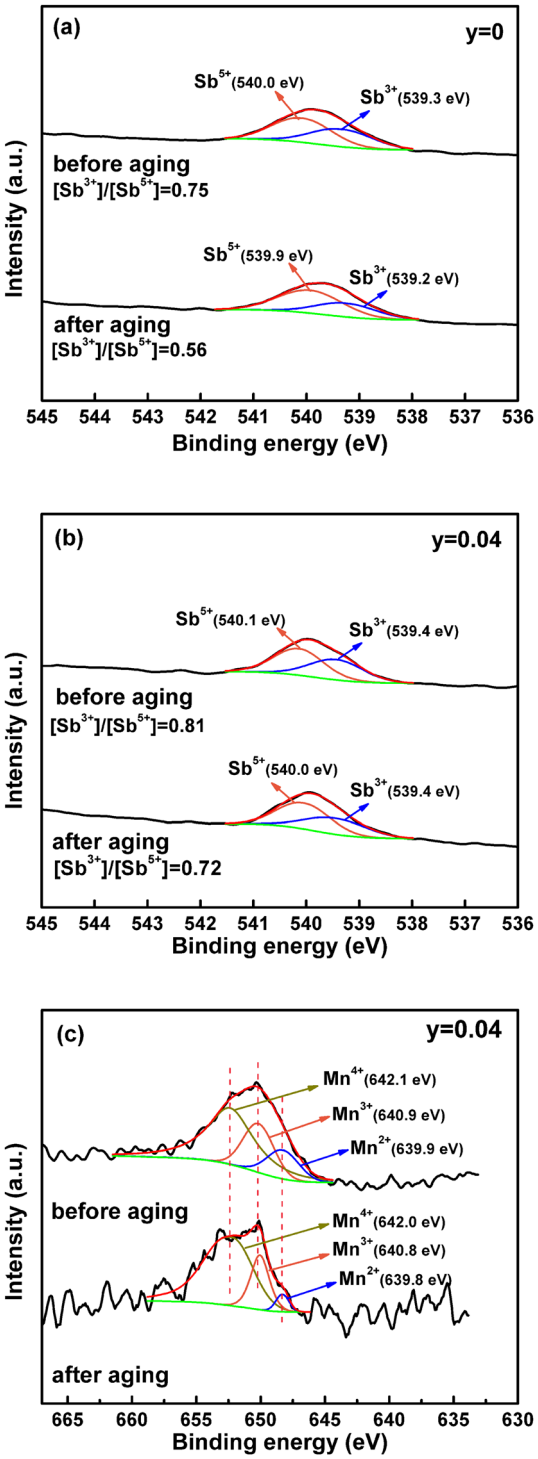

Fig. 7 XPS analysis of yMATO (y = 0, 0.04) ceramics before aging and after being aged for 500 h, **a** Sb $3d_{3/2}$ spectra for y = 0, **b** Sb $3d_{3/2}$ spectra for y = 0.04, **c** Mn $2p_{3/2}$ spectra for y = 0.04

reaction. All the ceramics have tetragonal rutile-type SnO_2 phase. Sb dopants can enhance the electrical conductivity of SnO_2 ceramic by orders of magnitude, but the $Sn_{1-x}Sb_xO_2$ ceramics shows lower temperature sensitivity. The $Sn_{0.95-y}Sb_{0.05}Mn_yO_2$ ceramics exhibit typical NTC characteristic, and room-temperature resistivity ρ_{25} and temperature sensitivity $B_{25/85}$ are adjusted in a large range. The $Sn_{0.91}Sb_{0.05}Mn_{0.04}O_2$ ceramic shows the lowest resistance change rate of 0.6% after being aged in air for 500 h, while $Sn_{0.95}Sb_{0.05}O_2$ ceramic has resistance change rate of − 14.29%. The aging induced resistance drift originated from the oxidation of Sb ion. The appropriate amount of Mn ions doping can restrain the conversion process from Sb^{3+} to Sb^{5+} and show more stable electrical property. The unique merit of controllable ρ_{25} and $B_{25/85}$ value and high electrical stability make the Sb/Mn co-doped SnO_2 ceramics suitable for NTC thermistors.

Acknowledgements

This work is supported by research funds from the National Natural Science Foundation of China (No. 51767021), Key Area Research and Development Program of Guangdong Province, China (No. 2019B090913002), and Hunan Wedid Materials Technology Co., Ltd., China (No. 738010241).

Declarations

Conflict of interest The authors declare that they have no known competing financial interests or personal relationships that could have appeared to influence the work reported in this paper.

References

1. A. Feteira, Negative temperature coefficient resistance (NTCR) ceramic thermistors: an industrial perspective. J. Am. Ceram. Soc. **92**, 967–983 (2009)
2. A. Feteira, K. Reichmann, NTC ceramics: past, present and future. Adv. Sci. Technol. **67**, 124–133 (2010)
3. P. Atanasijevic, P. Mihailovic, Temperature compensation of NTC thermistors based anemometer. Sens. Actuator A-Phys. **285**, 210–215 (2019)
4. Y. Zhao, S.S. Berbano, L. Gao, K. Wang, J. Guo, K. Tsuji, J. Wang, C.A. Randall, Cold-sintered V_2O_5-PEDOT: PSS nanocomposites for negative temperature coefficient materials. J. Eur. Ceram. Soc. **39**, 1257–1262 (2019)
5. B. Yang, Y. Feng, X. Deng, S. Ta, D. Xiong, M. He, RuO_2 doping and its influence on phase structure, cations state, and

electrical properties of $Mn_{1.6}Co_{0.4}CuO_4$ ceramics. Ceram. Int. **47**, 2107–2114 (2021)
6. H. Gao, C. Ma, B. Sun, Preparation and characterization of $NiMn_2O_4$ negative temperature coefficient ceramics by solid-state coordination reaction. J. Mater. Sci.-Mater. Electron. **25**, 3990–3995 (2014)
7. J. Guo, H. Zhang, Z. He, S. Li, Z. Li, Electrical properties and temperature sensitivity of Mo-modified $MnFe_2O_4$ ceramics for application of NTC thermistors. J. Mater. Sci.-Mater. Electron. **29**, 2491–2499 (2018)
8. W. Kong, W. Wei, B. Gao, A. Chang, A study on the electrical properties of Mn-Co-Ni-O thin films grown by radio frequency magnetron sputtering with different thicknesses. Appl. Surf. Sci. **423**, 1012–1018 (2017)
9. Q. Wang, W. Kong, J. Yao, A. Chang, Fabrication and electrical properties of the fast response $Mn_{1.2}Co_{1.5}Ni_{0.3}O_4$ miniature NTC chip thermistors. Ceram. Int. **45**, 378–383 (2019)
10. H. Han, K.R. Park, Y. Hong, K. Shim, S. Mhin, Effect of Fe incorporation on cation distributions and hopping conductions in Ni-Mn-Co-O spinel oxides. J. Alloys. Compd. **732**, 486–490 (2018)
11. K. Park, K.J. Lee, The effect of ZnO content and sintered temperature on the electrical properties of Cu-containing $Mn_{19.5-x}Ni_{0.45}Co_{0.15}Cu_{0.45}Zn_xO_4$ NTC thermistors. J. Alloys Compd. **475**, 513–517 (2009)
12. H. Li, H. Zhang, S. Thayil, A. Chang, X. Sang, X. Ma, Enhanced aging and thermal shock performance of $Mn_{19.5-x}CO_{0.21}Ni_{0.84}Sr_xO_4$ NTC ceramics. J. Adv. Ceram. **10**, 258–270 (2021)
13. H. Li, H. Zhang, A. Chang, X. Ma, J. Rong, L. Yang, A novel core-shell structure NTC ceramic with high stability fabricating by an in-situ ink-jet printing method. J. Eur. Ceram. Soc. **41**, 4167–4174 (2021)
14. B. Wang, J. Wang, A. Chang, J. Yao, Effects of particle sizes of starting oxides on the properties of spinel-type $Mn_{1.1-x}Co_{1.5}Fe_{0.4}O_4$ negative temperature coefficient ceramics. Ceram. Int. **47**, 2531–2537 (2021)
15. M. Zhao, W. Chen, W. Wu, M. Zhang, Z. Li, Aging characteristic of Cu-doped nickel manganite NTC ceramics. J. Mater. Sci.-Mater. Electron. **31**, 11784–11790 (2020)
16. M. Cui, X. Zhang, K. Liu, H. Li, M. Gao, S. Liang, Fabrication of nano-grained negative temperature coefficient thermistors with high electrical stability. Rare Met. **40**, 1014–1019 (2021)
17. T. Battault, R. Legros, A. Rousset, Aging of iron manganite negative temperature coefficient thermistors. J. Mater. Res. **13**, 1238–1242 (1998)
18. W.A. Groen, C. Metzmacher, V. Zaspalis, P. Huppertz, S. Schuurman, Aging of NTC ceramics in the system Mn-Ni-Fe-O. J. Eur. Ceram. Soc. **21**, 1793–1796 (2001)
19. D. Li, S. Zhao, K. Xiong, H. Bao, C. Nan, Aging improvement in Cu-containing NTC ceramics prepared by co-precipitation method. J. Alloys. Compd. **582**, 283–288 (2014)
20. Z. Wang, C. Zhao, P. Yang, L. Winnubst, C. Chen, Effect of annealing in O_2 or N_2 on the aging of $Fe_{0.5}Mn_{1.84}Ni_{0.66}O_4$ NTC ceramics. Solid State Ionics. **177**, 2191–2194 (2006)
21. R. Metz, Electrical properties of NTC thermistors made of manganite ceramics of general spinel structure: $Mn_{3-x-x'}M_xN_{x'}O_4$ ($0 \le x+x' \le 1$; M and N being Ni, Co or Cu). Aging phenomenon study. J. Mater. Sci. **35**, 4705–4711 (2000)
22. H. Li, I.P.L. Thayil, X. Ma, X. Sang, H. Zhang, A. Chang, Electrical properties and aging behavior of Na-doped $Mn_{1.95}Co_{0.21}Ni_{0.84}O_4$ NTC ceramics. Ceram. Int. **46**, 24365–24370 (2020)
23. F. Guan, Z. Dang, S. Huang, J. Wang, I. Milisavljevic, D. Carloni, X. Cheng, Y. Wu, $LaCr_{1-x}Fe_xO_3$ ($0 \le x \le 0.7$): a novel NTC ceramic with high stability. J. Eur. Ceram. Soc. **40**, 5597–5601 (2020)
24. P. Ouyang, H. Zhang, Y. Zhang, J. Wang, Z. Li, Zr-substituted SnO_2-based NTC thermistors with wide application temperature range and high property stability. J. Mater. Sci.-Mater. Electron. **26**, 6163–6169 (2015)
25. B. Yang, H. Zhang, J. Guo, Y. Liu, Z. Li, Electrical properties and thermal sensitivity of Ti/Y modified CuO-based ceramic thermistors. Front. Mater. Sci. **10**, 413–421 (2016)
26. P. Li, H. Zhang, C. Gao, G. Jiang, Z. Li, Electrical property of Al/La/Cu modified ZnO-based negative temperature coefficient (NTC) ceramics with high ageing stability. J. Mater. Sci.-Mater. Electron. **30**, 19598–19608 (2019)
27. Z. Yang, H. Zhang, Z. He, B. Li, Z. Li, Influence of B^{3+} and Na^+ ions on electrical property and temperature sensitivity of NiO-based ceramics. J. Mater. Sci.-Mater. Electron. **30**, 3088–3097 (2019)
28. C. Gao, Z. Li, L. Yan, D. Peng, H. Zhang, Investigation of electrical and aging properties of Bi-modified $(Zn_{0.4}Ni_{0.6})_{1-x}Na_xO$ ceramic thermistors. J. Eur. Ceram. Soc. **41**, 4160–4166 (2021)
29. Y. Zhang, Y. Wu, H. Zhang, W. Chen, G. Wang, Z. Li, Characterization of negative temperature coefficient of resistivity in $(Sn_{1-x}Ti_x)_{0.95}Sb_{0.05}O_2$ ($x \le 0.1$) ceramics. J. Mater. Sci.-Mater. Electron. **25**, 5552–5559 (2014)
30. J. Zhang, H. Zhang, B. Yang, Y. Zhang, Z. Li, Temperature sensitivity of Fe-substituted SnO_2-based ceramics as negative temperature coefficient thermistors. J. Mater. Sci.-Mater. Electron. **27**, 4935–4942 (2016)

31. W. Yan, H. Zhang, X. Wang, C. You, Z. Li, Characterization of electrical conductivity and temperature sensitivity of Cr/Sb-modified SnO_2 ceramics. J. Mater. Sci.-Mater. Electron. **31**, 4040–4049 (2020)
32. I. Ahmad, M.J. Akhtar, R.T.A. Khan, M.M. Hasan, Change of Mott variable range to small polaronic hole hopping conduction mechanism and formation of Schottky barriers in $Nd_{0.9}Sr_{0.1}FeO_3$. J. Appl. Phys. **114**, 34103 (2013)
33. X. Xie, J. Wang, L. Chen, Z. Hu, S. Yan, A. Chang, Effect of sintering temperature on thermal stability of $Zn_{0.2}Fe_{1.05}NiMn_{0.75}O_4$ ceramic materials by homogeneous co-precipitation method. J. Mater. Sci.-Mater. Electron. **28**, 190–196 (2017)
34. M. Guan, J. Yao, W. Kong, J. Wang, A. Chang, Effects of Zn-doped on the microstructure and electrical properties of $Mn_{1.5-x}Co_{1.2}Cu_{0.3}Zn_xO_4$ ($0 \leq x \leq 0.5$) NTC ceramics. J. Mater. Sci.-Mater. Electron. **29**, 5082–5086 (2018)
35. W. Ren, N. Zhu, L. Li, H. Feng, Y. Wang, Y. Yang, Z. Yang, S. Shang, Improvement of ageing issue in $Zn_{0.4}Fe_{2.1}Co_2Mn_{1.5}O_8$ thermistor films. J. Eur. Ceram. Soc. **39**, 4189–4193 (2019)
36. M. Li, P. Cheng, G. Luo, J.M. Schoenung, Q. Shen, Effects of Sb oxidation state on the densification and electrical properties of antimony-doped tin oxide ceramics. J. Mater. Sci.-Mater. Electron. **26**, 4015–4020 (2015)
37. M.C. Biesinger, B.P. Payne, A.P. Grosvenor, L.W.M. Lau, A.R. Gerson, R.S.C. Smart, Resolving surface chemical states in XPS analysis of first row transition metals, oxides and hydroxides: Cr, Mn, Fe, Co and Ni. Appl. Surf. Sci. **257**, 2717–2730 (2011)
38. W. Dai, X. Pan, C. Chen, S. Chen, W. Chen, H. Zhang, Z. Ye, Enhanced UV detection performance using a Cu-doped ZnO nanorod array film. RSC. Adv. **4**, 31969–31972 (2014)